

Radio Interferometric Studies of Cool Evolved Stellar Winds

A dissertation submitted to the University of Dublin
for the degree of Doctor of Philosophy

Eamon O’Gorman

Supervisor: Dr. Graham M. Harper

Trinity College Dublin, September 2013

SCHOOL OF PHYSICS
UNIVERSITY OF DUBLIN
TRINITY COLLEGE



Declaration

I declare that this thesis has not been submitted as an exercise for a degree at this or any other university and it is entirely my own work.

I agree to deposit this thesis in the University's open access institutional repository or allow the library to do so on my behalf, subject to Irish Copyright Legislation and Trinity College Library conditions of use and acknowledgement.

Name: Eamon O'Gorman

Signature: **Date:**

Summary

Mass-loss becomes significant for most stars as they approach the end of their lives and become either red giants or red supergiants. This continuous mass-loss, which occurs in the form of a relatively dense and slow-moving wind, can have a significant impact on the evolution of gas and dust in galaxies, on surrounding planets, and indeed on the very evolution of the star itself. Despite the importance of this phenomenon and decades of study, the fundamental mechanisms responsible for producing these winds remain unknown. The main reason for this is due to our lack of understanding of the dynamics and thermodynamics of the stellar outflow environment. Isolated giants and supergiants do not contain the expected additional complexities encountered by binaries, making them ideal targets for understanding the nature of these outflows. Traditionally, observations have provided only limited disk-averaged information about the outflow environments of these stars making it difficult to infer the outflow properties. However, the latest suite of radio interferometers now have the capability to provide essential spatial information on these outflow environments.

This thesis first presents the results of a radio interferometric study into the dynamics of the two unique flows in the circumstellar environment of the M2 red supergiant, Betelgeuse. The Combined Array for Research in Millimeter-wave Astronomy (CARMA) was used in multiple configurations to observe the CO($J = 2 - 1$) emission line allowing spatial scales as small as $0''.9$ to be traced over a $32''$ field of view. The outer flow known as S2, was found to have outflow velocities of -15.4 and $+13.2 \text{ km s}^{-1}$ with respect to the stellar rest frame and

extend out to $17''$, while the inner flow known as S1, was found to have outflow velocities of -15.4 and $+13.2 \text{ km s}^{-1}$ and extend out to $4 \rightarrow 6''$. Both flows were found to be inhomogeneous down to the resolution limit, but when azimuthally averaged, their intensity falloff was found to be consistent with an optically thin, spherically symmetric constant velocity outflow. High resolution multi-epoch centimeter continuum observations of Betelgeuse which probe its inner atmosphere ($\sim 1-5 R_*$) are also presented. The radio flux density is found to vary on time scales of $\lesssim 14$ months at all wavelengths, and again evidence for inhomogeneities in the outflow is found.

This thesis also presents Karl G. Jansky Very Large Array (VLA) multi-wavelength ($0.7 - 20 \text{ cm}$) observations of two non-dusty, non-pulsating K spectral-type red giants, Arcturus and Aldebaran. Detections at 10 cm (3.0 GHz : S-band) and 20 cm (1.5 GHz : L-band) represent the first isolated luminosity class III red giants to be detected at these long wavelengths. These thermal continuum observations provide a snapshot of the different stellar atmospheric layers and are independent of any long-term variability. The long wavelength data sample Arcturus' outer atmosphere where its wind velocity is approaching its terminal value and the ionization balance is becoming *frozen-in*. For Aldebaran the data still sampling its inner atmosphere where the wind is still accelerating. Our data is in conflict with published semi-empirical models based on ultraviolet data. Spectral indices are used to discuss the possible properties of the stellar atmospheres. Evidence for a rapidly cooling wind in the case of Arcturus is found and a new analytical wind model is developed for this star. This model is used as the basis to compute a thermal energy balance of Arcturus' outflow by investigating the various heating and cooling processes that control its thermal structure. The analysis focuses on distances between $1.2 \rightarrow 10 R_*$ and includes the wind acceleration zone. We find that an additional substantial heating mechanism is required to maintain the inner thermal structure of the outflow.

*For Mum and Dad,
a constant source of inspiration and guidance.*

Acknowledgements

Some sincere acknowledgements...

List of Publications

Refereed

1. **O’Gorman, E.**, Harper, G. M., Brown, A., Brown, A., Drake, S., and Richards, A. M. S.
“Multi-wavelength Radio Continuum Emission Studies of Dust-free Red Giants”
The Astronomical Journal, 146, 98, (2013)
2. Richards, A. M. S., Davis, R. J., Decin, L., Etoke, S., Harper, G. M., Lim, J. J., Garrington, S. T., Gray, M. D., McDonald, I., **O’Gorman, E.**, Wittkowski, M.
“e-MERLIN resolves Betelgeuse at wavelength 5 cm”
Monthly Notices of the Royal Astronomical Society Letters, 432, L61 (2013)
3. **O’Gorman, E.**, Harper, G. M., Brown, J. M., Brown, A., Redfield, S., Richter, M. J., and Requena-Torres, M. A.
“CARMA CO(J = 2 - 1) Observations of the Circumstellar Envelope of Betelgeuse”
The Astronomical Journal, 144, 36 (2012)
4. Sada, P. V., Deming, D., Jennings, D. E., Jackson, B. K., Hamilton, C. M., Fraine, J., Peterson, S. W., Haase, F., Bays, K., Lunsford, A., and **O’Gorman, E.**
“Extrasolar Planet Transits Observed at Kitt Peak National Observatory”
Publications of the Astronomical Society of the Pacific, 124, 212 (2012)

-
5. Sada, P. V., Deming, D., Jackson, B. K., Jennings, D. E., Peterson, S. W., Haase, F., Bays, K., **O’Gorman, E.**, and Lundsford, A.
“Recent Transits of the Super-Earth Exoplanet GJ 1214b”
The Astrophysical Journal Letters, 720, L215 (2010)

Non-Refereed

1. **O’Gorman, E.**, & Harper, G. M.
“What is Heating Arcturus’ Wind?”,
Proceedings of the 16th Cambridge Workshop on Cool Stars, Stellar Systems and the Sun. Astronomical Society of the Pacific Conference Series, 448, 691 (2011)

Contents

List of Publications	vii
List of Figures	x
List of Tables	xi
1 Introduction to Radio Interferometry	1
1.1 Radio Antenna Fundamentals	1
1.1.1 Properties of a Radio Antenna	2
1.1.2 Antenna Structural Design	5
1.1.3 Antenna Performance Parameters	7
1.2 Receiving System for an Interferometer	9
1.3 Fundamentals of Radio Interferometry	11
1.3.1 Young’s Slits	11
1.3.2 The Two-element Interferometer	13
1.3.3 Complex Visibility	17
1.3.4 Coordinate Systems for Imaging	18
1.4 Synthesis Imaging	19
1.4.1 Visibility Sampling	20
1.4.2 Imaging (Making a Dirty Map)	21
1.4.3 Deconvolution (Making a CLEAN map)	23
A List of Abbreviations Used in this Thesis.	26
References	28

List of Figures

1.1	Radiation and power pattern of a uniformly illuminated antenna.	4
1.2	Common optical systems used for radio antennas.	7
1.3	Block diagram of a superheterodyne receiver.	10
1.4	Fringe pattern produced by Young's slits under various situations.	12
1.5	Visibilities for various source sizes.	14
1.6	Simplified schematic diagram of a two-element interferometer. . .	15
1.7	The instantaneous point source responses of an interferometer. . .	16
1.8	The (u, v, w) interferometric coordinate system.	20
1.9	VLA antenna layout and two examples of $u - v$ coverage for different track lengths.	21
1.10	The Fourier transform pairs in synthesis imaging.	23

List of Tables

A.1 List of Abbreviations 26

1

Introduction to Radio Interferometry

The poor spatial resolution provided by a single dish radio antenna can cause difficulties in obtaining accurate flux density measurements of radio astronomical sources, especially at long wavelengths. A single dish radio antenna is unable to distinguish against background radio emitters located in the primary beam, and therefore the observed flux density can contain emission from unrelated sources. This limitation can be overcome through interferometry. An interferometer acts as a spatial filter, and can discriminate against smooth backgrounds, while its higher resolution allows separation of the target from nearby confusing sources. The chapter describes the basic elements of a radio interferometer, what happens to the radio signal before it is sent for correlation, introduces the general concept of interferometry, and explains the process of synthesis imaging.

1.1 Radio Antenna Fundamentals

The quality and properties of the final radio image produced from a synthesis array are partially dependent on the properties of the individual antennas in the array. The most important such properties are discussed in the following sections and include aperture size, aperture efficiency, pointing accuracy and sidelobe

level. We define the radio antenna as the piece of equipment which converts the electromagnetic waves emitted from the observed source into an electric current ready to be input into the first low noise amplifier where the signal is at the radio/sky frequency, ν_{RF} . What happens to the signal after this will be discussed in Section 1.2.

1.1.1 Properties of a Radio Antenna

The power gain of a transmitting antenna is a measure of the antenna's capability of converting power into radio waves in a specific direction. In radio astronomy, the receiving counterpart of transmitting power gain is the effective collecting area of an antenna, $A(\nu, \theta, \phi)$, where ν is frequency and θ and ϕ are direction coordinates. An ideal radio antenna would collect all incident radiation from a distant point source and convert it to electrical power. The total spectral power P_ν collected by it would then be a product of its geometric area and the incident spectral power per area, or flux density F_ν . By analogy then, the effective area of a real radio antenna is defined

$$A(\nu, \theta, \phi) = \frac{P_\nu}{F_\nu} = \frac{P}{I(\nu, \theta, \phi) \Delta\nu \Delta\Omega} \quad (1.1)$$

where $I(\nu, \theta, \phi)$ is the source brightness in units $\text{W m}^{-2} \text{Hz}^{-1} \text{sr}^{-1}$ that the antenna is pointing at and P is the power (in Watts) received by the antenna in bandwidth $\Delta\nu$ from element $\Delta\Omega$ of solid angle. The normalized antenna reception pattern \mathcal{A} , often referred to as the power pattern due to the duality between receiving and transmitting, is defined as

$$\mathcal{A}(\nu, \theta, \phi) = \frac{A(\nu, \theta, \phi)}{A_0} \quad (1.2)$$

where A_0 (m^2) is often referred to as the effective area of the antenna and is the response at the center of the main lobe of $A(\nu, \theta, \phi)$ [i.e., $A(\nu, 0, 0)$]. Then the beam solid angle, Ω_A , of the primary beam is

$$\Omega_A = \iint_{\text{all sky}} \mathcal{A}(\theta, \phi) d\Omega \quad (1.3)$$

and is a measure of the field of view of the antenna.

1.1 Radio Antenna Fundamentals

In the case of an isotropic antenna [i.e., $\mathcal{A}(\nu, \theta, \phi) = 1$], it can be shown that the product of the effective area and the primary beam solid angle is equal to the square of the wavelength (Kraus *et al.*, 1986)

$$A_0 \Omega_A = \lambda^2. \quad (1.4)$$

Ω_A has its maximum possible value of 4π if \mathcal{A} is everywhere equal to 1. This means that the primary antenna can see the whole sky with equal sensitivity. Even though a large field of view is usually desirable in radio astronomy, Equation 1.4 ensures that for any given wavelength, when Ω_A is a maximum, the power received is a minimum and therefore the sensitivity is also at a minimum. To improve sensitivity, one could increase the collecting area of the antenna, but Equation 1.4 then ensures that the field of view must decrease. Thus, when deciding on the primary antenna size in a synthesis array, there is always a trade-off between field of view and sensitivity.

In reality, an antenna cannot radiate isotropically and will radiate preferentially in one or more directions. A Fourier transform relationship exists between the complex voltage distribution of the field, $f(u, v)$, in the aperture of the antenna and the complex far-field voltage radiation pattern, $F(l, m)$, of the antenna (Kraus *et al.*, 1986)

$$F(l, m) = \iint_{\text{aperture}} f(u, v) e^{2\pi i(ul+vm)} du dv \quad (1.5)$$

and

$$f(u, v) = \int_{-\infty}^{\infty} \int_{-\infty}^{\infty} F(l, m) e^{-2\pi i(ul+vm)} dl dm \quad (1.6)$$

where

$$u = \sin\theta\cos\phi \quad \text{and} \quad v = \sin\theta\sin\phi \quad (1.7)$$

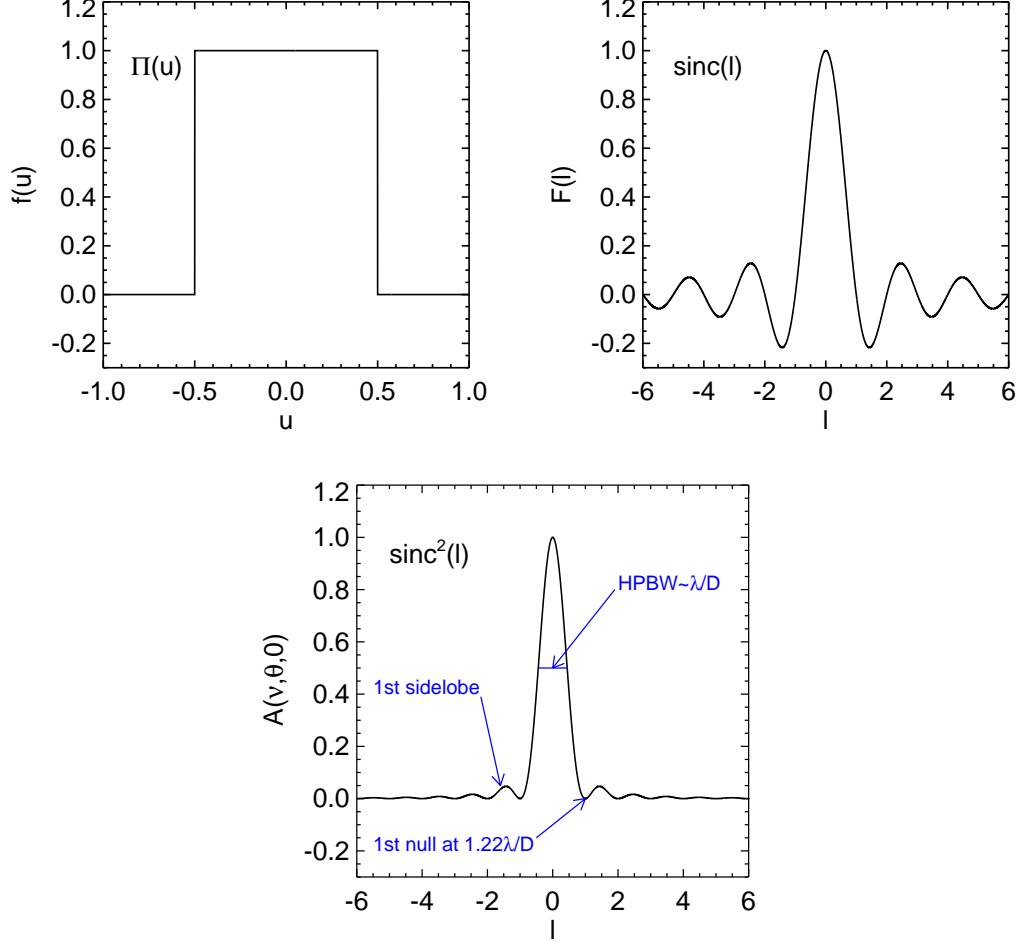


Figure 1.1: *Top Left:* A uniformly illuminated 1-D aperture $f(u)$. *Top Right:* The Fourier transform of $f(u)$ gives the antenna radiation pattern in the far-field, $F(l)$. *Bottom:* The power pattern of the antenna is given by $\mathcal{A} = |F(l)|^2$.

are the antenna coordinates and l and m are their Fourier counterparts. The form of $f(u, v)$ is determined by the manner in which the antenna feed illuminates the aperture. Therefore Equations 1.6 and 1.7 tell us that the radiation pattern in the far-field of a two-dimensional aperture is the two-dimensional Fourier transform of the aperture field illumination. For a uniformly illuminated 1-D aperture shown in Figure 1.1, the radiation pattern in the far-field is the *sinc* function. The radiation pattern in the far-field, $F(l, m)$, of such an antenna is related to the antenna power pattern by $\mathcal{A} = |F(l, m)|^2$. This power pattern is known as the Airy pattern if the antenna is uniformly illuminated and is also shown in Figure

1.1. The central peak of this power pattern is called the main beam while the smaller secondary peaks are called sidelobes. The antenna is maximally sensitive to radiation from the direction of the peak of the beam, but is also slightly sensitive to radiation in the direction of the side lobes. The half-power beamwidth (HPBW) of the main beam θ_{HPBW} is a term commonly used in the literature to describe the field of view of an antenna/interferometer and satisfies

$$\theta_{\text{HPBW}} \propto \frac{\lambda}{D} \quad (1.8)$$

where D is the diameter of the antenna. The constant of proportionality varies slightly with the illumination taper and can be shown to be equal to ~ 0.89 for a uniformly illuminated 1-D aperture and ~ 1.2 for most single dish radio antennas. When the sky is scanned with a single dish antenna, then this HPBW is the resolution of the resulting map.

1.1.2 Antenna Structural Design

The design of the primary antenna element of an interferometric array will depend on the wavelength range to be observed. In general, dipoles are used for wavelengths longer than ~ 1 m, while reflector antennas are typically used at shorter wavelengths. The reason why the more simple and less expensive dipoles are not used at all wavelengths is given by Equation 1.4. For an isotropic antenna, this equation tells us that the effective area is just

$$A_0 = \frac{\lambda^2}{4\pi}. \quad (1.9)$$

Therefore, at short wavelengths a non-directional antenna such as a dipole, will have a small effective collecting area, giving it poor sensitivity for reception. Thus, dipoles can be used at long wavelengths as they have sufficient collecting area, but cannot be used at shorter wavelengths as an impractical amount would be needed to produce useful collecting areas. Since the interferometric arrays used in this thesis use reflector antennas, the rest of this section will focus on them.

Choice of Antenna Mount. Nearly all interferometric arrays consist of antennas which have altitude over azimuth (alt-azimuth) mounts. These antennas lie on a horizontal azimuth track on which the antenna can turn in azimuth, and on a horizontal elevation axle about which the antenna can change in zenith angle. The main advantage of such a design is simplicity and thus lower cost. Gravity always acts on the reflector in the same plan thus reducing the problem of keeping the reflector profile accurate during the duration an observation. However, sources close to the zenith can usually not be observed due to the high rate of azimuth rotation required. Also, the beam rotates with respect to the source for long duration observations which can affect the dynamic range of total intensity images of very large sources. The other type of mount occasionally used is the equatorial mount. Its polar axis is aligned parallel to the axis of rotation of the Earth and therefore only needs to rotate about the declination axis to observe a source. Its beam also doesn't have the beam rotation problem encountered by the alt-azimuth design and can track sources close to the zenith. Its major disadvantage and the reason for its scarce usage is the complexity of its design and resulting increased cost.

Choice of Antenna Optics. In Figure 1.2 we show the main optical systems which can be used to feed a large radio reflector. The prime focus system (e.g. used in the Giant Meter Radio Telescope) has the advantage that it can be used at long wavelengths where the use of secondary focus feeds (i.e., sub-reflectors) become impractical. However, access to and space for the feeds and receivers are limited, and sensitivity can be lost due to spillover noise from the ground. The other designs have the advantage of easier access to the feeds and receivers and less spillover noise from the ground. The off-axis Cassegrain (e.g. used in the Very Large Array) also has the advantage of increased frequency capability as many feeds can be located in a circle around the center of the reflector and a slight rotation of the sub-reflector is all that is required to change observing frequency. The receivers and feeds in the Naysmith geometry (e.g. used in the Combined Array for Research in Millimeter wave Astronomy) are located externally to the antenna structure. Finally, the offset Cassegrain (e.g. used in the Green Bank Telescope)

has no blockage and will have a circularly symmetric beam with low sidelobes although the increase complexity of its structure leads to increased costs.

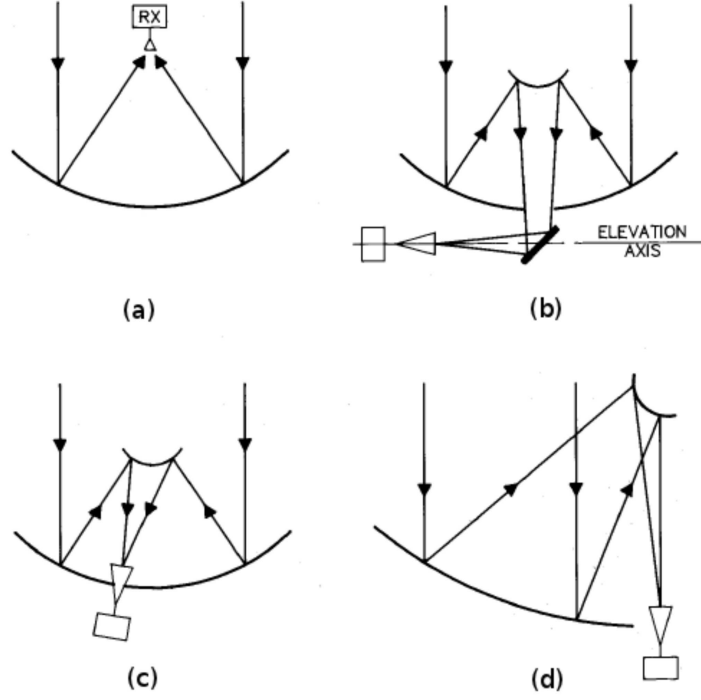


Figure 1.2: Common optical systems used for radio antennas. (a) Prime focus, (b) Naysmith, (c) Off-axis Cassegrain, (d) Offset Cassegrain [Figure adapted from Taylor *et al.* (1999)].

1.1.3 Antenna Performance Parameters

Aperture Efficiency. The geometric collecting area of a parabolic antenna A_{geo} ($= \pi D^2/4$) is related to the effective area (i.e., the collecting area when pointing directly at a source) via the dimensionless quantity η ($\eta < 1$) known as the aperture efficiency where

$$\eta = \frac{A_0}{A_{\text{geo}}}. \quad (1.10)$$

The aperture efficiency directly impacts on the sensitivity of the interferometric array and can be defined as the product of a number of different efficiency loss

factors,

$$\eta = \eta_{\text{sf}}\eta_{\text{bl}}\eta_{\text{s}}\eta_{\text{t}}\eta_{\text{misc}}. \quad (1.11)$$

The surface efficiency η_{sf} accounts for the aperture efficiency loss as a result of reflector profile inaccuracies. Such inaccuracies result in the electric field from various parts of the aperture not adding together in phase at the feed leading to a decrease in power. The aperture blockage efficiency η_{bl} accounts for the fact that the sub-reflector (or feed) and its support structure result in a reduction in the incident radiation on the antenna. The feed spillover efficiency η_{s} is best understood if the antenna is considered in transmission rather than in reception mode, and is defined as the fraction of power radiated by the feed that is intercepted by the reflector for a prime focus system, or by the sub-reflector for a Cassegrain system. The illumination taper efficiency η_{t} accounts for the fact that the feed pattern does not illuminate the primary reflector uniformly but illuminates the outer part of the reflector at a lower level than the inner part. Finally, the miscellaneous efficiency losses such as reflector diffraction and feed position phase errors are accounted for in η_{misc} . As an example, the total aperture efficiency of the VLA antennas can vary between 0.65 and 0.2 at 6 and 0.7 cm, respectively.

Pointing Accuracy. The main lobe of an antenna's power pattern will usually not point exactly in the desired direction due to gravity deformations, wind pressure deformations, and mechanical inaccuracy. The angular offset, $\Delta\theta$, between the actual and desired pointing direction is called the pointing error. Usually, the desirable pointing error of an antenna at the highest operational frequency is $\Delta\theta < \theta_{\text{HPBW}}/20$ (Taylor *et al.*, 1999). With this specification reached, an antenna pointing at a compact source will suffer negligible intensity variations as $\mathcal{A}(\theta_{\text{HPBW}}/20) > 0.99$. However, this pointing error of only $\theta_{\text{HPBW}}/20$ will still have a substantial effect on the accuracy of the outer image. For example, a source located at the half power point will suffer a substantial fractional intensity variation of $2\mathcal{A}(\theta_{\text{HPBW}}/2 + \theta_{\text{HPBW}}/20) \simeq 0.86$. The blind pointing of a VLA antenna is only about $10''$ and can be much worse in daytime, occasionally exceeding $1'$. This means that at Q-band (45 GHz; 0.7 cm), which is the highest observing frequency on the VLA, the pointing error is only at best $\theta_{\text{HPBW}}/6$, and

at worst $> \theta_{\text{HPBW}}$, meaning that the target may lie outside of the primary beam. To overcome this problem of large antenna pointing errors at high frequencies with the VLA, a technique known as referenced pointing is implemented. This technique will be discussed further in Chapter 3.

1.2 Receiving System for an Interferometer

A radiometer (a radio receiver) is a device used to measure the timed-averaged power of the noise coming from a radio telescope within a well-defined radio frequency (RF) range, $\nu_{\text{RF}} - \Delta\nu_{\text{RF}}/2 \rightarrow \nu_{\text{RF}} + \Delta\nu_{\text{RF}}/2$, where $\Delta\nu_{\text{RF}}$ is the bandwidth of the receiver and $\Delta\nu_{\text{RF}} < \nu_{\text{RF}}$. The simplest radiometer carries out the following tasks:

1. Filters the broadband noise coming from the antenna via a bandpass filter.
2. Multiplies the filtered voltage by itself (i.e., its output voltage is proportional to its input power).
3. Smooths out the rapidly fluctuating output of the detected voltage via a signal averager or integrator.
4. Measures the smoothed voltage.

In practice, radiometers are never as simple as those described above and nearly all practical radiometers are *superheterodyne* receivers which incorporate a number of additional steps to produce an output voltage.

The RF front end is the term used to describe all the circuitry between the feed horn and the lower intermediate frequency (IF) stage. The first task of the front end is to amplify the received signal. The radio signals we want to measure are generally very weak and therefore need to be initially amplified by many orders of magnitude so they are above the noise level in succeeding stages. However, the front end electronic components produce random electrical noise which will also get amplified by this large amount. Therefore the role of the pre-amplifier is to amplify the incoming signal from the antenna while adding as little noise as possible. For this reason, the pre-amplifier is often called a low noise amplifier

1.2 Receiving System for an Interferometer

(LNA) and are often cooled to very low temperatures to minimize the amount of noise contributed by the components.

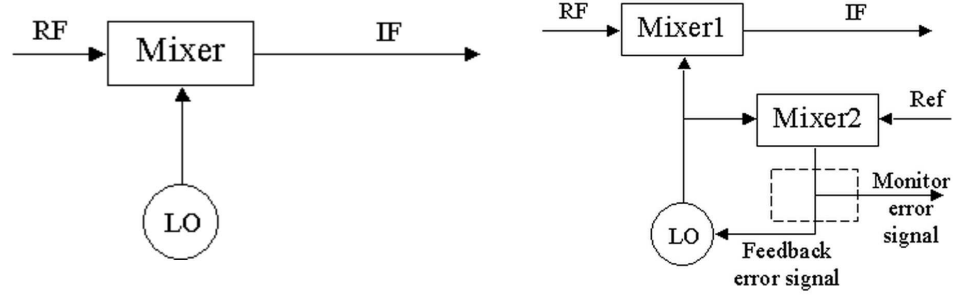


Figure 1.3: *Left:* Block diagram of a simple superheterodyne receiver. The amplified RF signal is mixed with a signal from a local oscillator to convert the signal to the more manageable intermediate frequency. *Right:* For interferometry, a phase lock loop is used to ensure all antennas are locked to the same frequency.

The amplified RF signal is then sent through a mixer which multiplies the RF signal by a sine wave of frequency ν_{LO} which is generated by a local oscillator (LO), as shown in Figure 1.3. The effect of this is that RF signal is changed to a lower frequency which can be easier handled by the IF amplifier and improves frequency selectivity. Mathematically, the mixer does the following

$$2\sin(2\pi\nu_{LO}t) \times \sin(2\pi\nu_{RF}t) = \cos[2\pi(\nu_{LO} - \nu_{RF})t] - \cos[2\pi(\nu_{LO} + \nu_{RF})t], \quad (1.12)$$

and produces two additional outputs, one at the input signal frequency minus the local oscillator frequency, and one at the sum of these frequencies. The lower of the two outputs called the intermediate frequency (IF) is taken by passing the mixer output through a filter in the IF amplifier. In interferometry, where the signals from two antennas are correlated, it is crucial that the receivers from both antennas are operating at the same frequency to control the phase difference between them. This is achieved by using a phase lock system, whose block diagram is laid out in Figure 1.3. In this system another mixer compares the LO to a reference frequency, which is the same for all antennas. Any existing phase error results in an error signal that is sent back to the oscillator so that its frequency can be adjusted to maintain exact frequency tuning. After this, the IF can finally be sent to the radiometer and recorded.

1.3 Fundamentals of Radio Interferometry

The angular resolution $\Delta\theta$ of a radio antenna is the minimum angular separation which two point sources can have in order to be recognized as separate objects. The *Rayleigh criterion* is the generally accepted criterion for defining the angular resolution of a filled circular aperture of diameter D , at the observational wavelength λ and is given as

$$\Delta\theta = 1.22 \frac{\lambda}{D} \text{ rad.} \quad (1.13)$$

The Rayleigh criterion states that two objects are resolved when the first null of the diffraction pattern of one object coincides with the maximum of the diffraction pattern of the other. An immediate consequence of Equation 1.13 is that at large wavelengths, the angular resolution becomes large unless the diameter of the aperture can be increased substantially. In order to achieve modest angular resolution at radio wavelengths with a single radio antenna then, the diameter becomes impractically large. For example, in order to achieve an angular resolution of $1''$ at 6 cm a 12 km aperture would be required. Radio interferometry is a technique used in radio astronomy to overcome this problem of poor angular resolution at long wavelengths.

1.3.1 Young's Slits

The basic principles of interferometry can be understood through Young's double-slit experiment. If coherent radiation emitted from a distant point source propagates through two slits, an illumination pattern composed of bright and dark fringes is observed. The phenomenon is a result of the constructive and destructive interference between the secondary waves produced by the slits. The fringe separation is λ/B , where B is the projected separation of the slits and is called the baseline. The fringe contrast which is historically known as the fringe visibility, V , can be written as

$$|V| = \frac{I_{\max} - I_{\min}}{I_{\max} + I_{\min}} \quad (1.14)$$

where I_{\max} and I_{\min} are the maximum and minimum intensity of the fringes, respectively. In other words, the fringe visibility is the fringe amplitude normalized

by the sum of the maximum and minimum intensity.

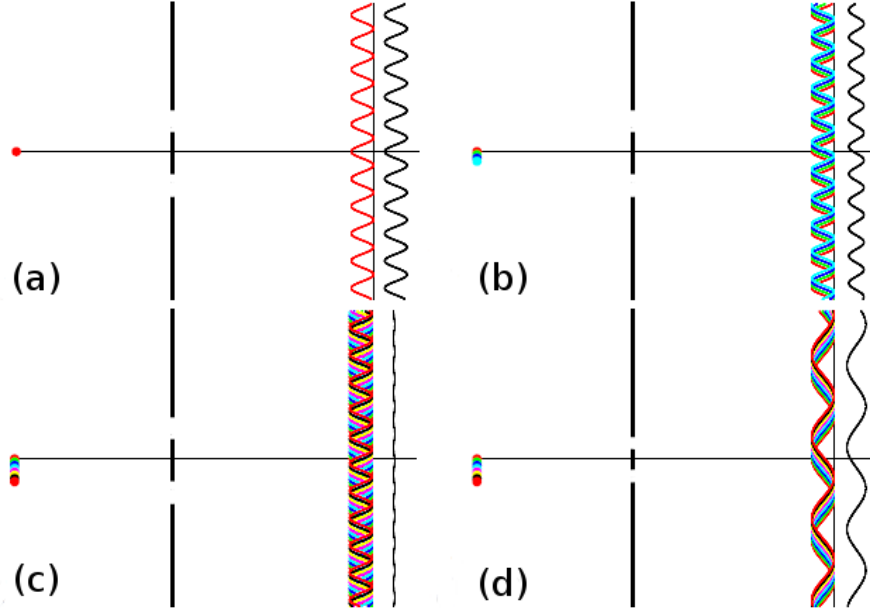


Figure 1.4: The resulting fringe pattern produced by Young’s slits under various conditions. The source is shown on the left of the slits in each panel, while the separate fringe patterns (colors) along with the added fringe pattern (black) is shown on the right of the slits. (a) Point source at infinity, (Visibility = 1). Fringes are separated by an angular distance of λ/B . (b) An increase in source size results in a drop in visibility. (c) When the source size is equal to λ/B , the visibility is zero. (d) If the source size remains the same as in (c) and the slit spacing is reduced, then the fringes re-appear. Figure adapted from [Jackson \(2008\)](#).

In the simple case shown in Figure 1.4a, the angular size of the source is $\ll \lambda/B$ and the fringe visibility is 1. In interferometry, this equates to the situation in which the source size is smaller than the synthesized beam and only an upper limit of the source size can be obtained (i.e., the source is unresolved). In Figure 1.4b, the angular size of the source is now larger and can be thought of as a sequence of point sources each emitting radiation which is uncorrelated with emission from the others. An angular shift of ϕ , called phase, in the sources position results in a shift in the corresponding fringe pattern by the same angle the other way. The total interference intensity pattern is then just the sum of these individual patterns and the visibility is reduced. When the extension of the

1.3 Fundamentals of Radio Interferometry

source equals λ/B , the fringes disappear and give a constant illumination pattern. In this case the fringe visibility is zero and the source is completely resolved as shown in Figure 1.4c. Finally, if the source size is the same as that in Figure 1.4c but the slit separation is reduced, then the fringe separation λ/B will again increase as shown in Figure 1.4d. This is because the source now produces much less displacement of the fringe patterns as a fraction of the fringe separation. In interferometry, this result means that extended sources can only be probed with short baselines.

Visibility and phase are often expressed together as the complex visibility $V = |V|e^{i\phi}$, which completely defines a pattern of interference fringes. Young's double-slit experiment demonstrates a fundamental property of interferometry, namely that the contrast of fringes is a function of the geometry of the source. The results of the experiment are summarized in Figure 1.5. The top row shows that a large source (i.e., one whose intensity distribution extends out to a large angle on the sky) has a fringe visibility pattern which falls off quickly as projected baseline length increases. The bottom row shows that for compact sources the fringe visibility remains high out to large baselines. In the following section we will show that the relationship between the sky brightness distribution $I(\theta)$ and the visibility $V(B)$ is a Fourier transform.

1.3.2 The Two-element Interferometer

Interferometers with N antennas can be treated as $N(N - 1)/2$ independent interferometer pairs so it is worthwhile studying the simplest case of the two-element interferometer. A simplified block diagram of the components of such an interferometer is shown in Figure 1.6. The figure shows two identical antennas separated by a baseline vector \mathbf{b} pointing towards a distant radio source in a direction indicated by the unit vector \mathbf{s} . The plane waves from the distant radio source reach antenna 1 at a time τ_g later than they reach antenna 2. τ_g is called the geometric delay and is given by

$$\tau_g = \frac{\mathbf{b} \cdot \mathbf{s}}{c} = \frac{b \cos \theta}{c} \quad (1.15)$$

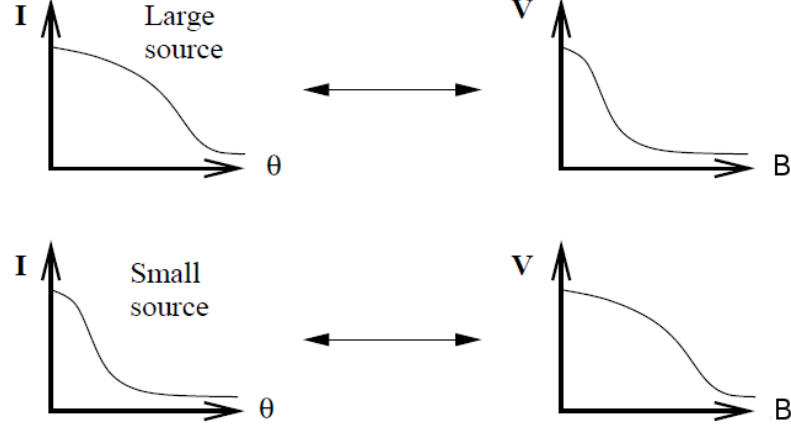


Figure 1.5: *Left column:* Intensity distribution as a function of sky angle for an extended source (top) and for a more compact source (bottom). *Right column:* The corresponding fringe visibility as a function of slit separation or baseline. Figure adapted from [Jackson \(2008\)](#).

where c is the speed of light. If we assume that the interferometer only responds to a very narrow band centered on frequency $\nu = \omega/2\pi$, then the output voltages of antennas 1 and 2 at time t can be written as

$$V_1(t) = V \cos[\omega(t - \tau_g)] \quad \text{and} \quad V_2(t) = V \cos(\omega t). \quad (1.16)$$

The signals are then passed through a correlator which first multiplies these voltages to give

$$V_1(t)V_2(t) = \frac{V^2}{2} [\cos(2\omega t - \omega\tau_g) + \cos(\omega\tau_g)] \quad (1.17)$$

and then averages them over a time interval Δt which is long enough such that $\Delta t \gg (2\omega)^{-1}$ to give the final output R :

$$R = \langle V_1(t)V_2(t) \rangle = \frac{V^2}{2} [\cos(\omega\tau_g)]. \quad (1.18)$$

As the Earth rotates, τ_g varies slowly with time and the resultant oscillations in the correlator output voltage represent the motion of the source. These

1.3 Fundamentals of Radio Interferometry

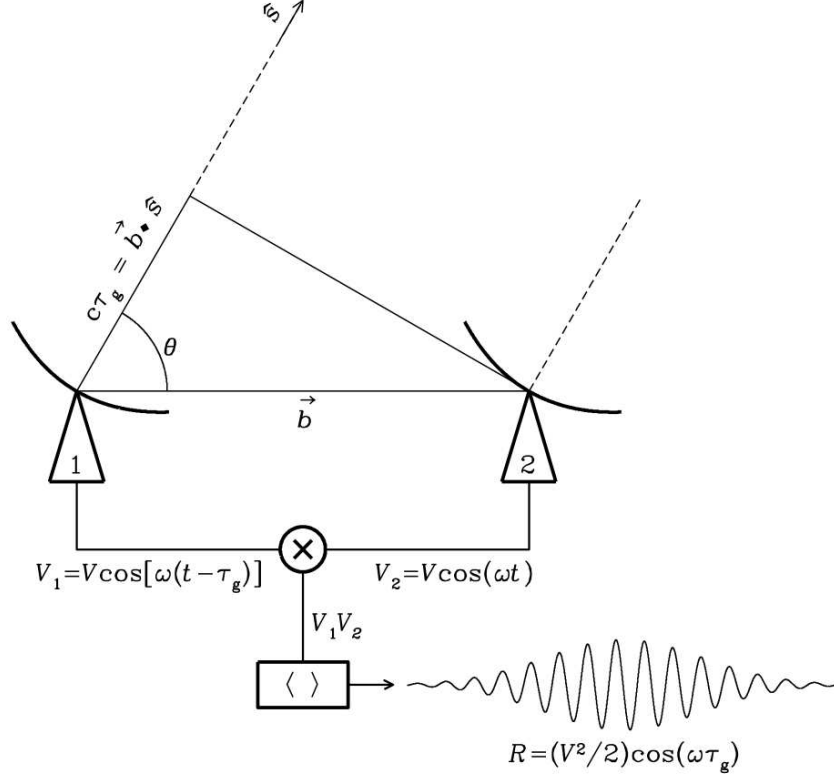


Figure 1.6: Simplified schematic diagram of a two-element interferometer. The correlator multiplies and averages the voltage outputs V_1 and V_2 of the two dishes and yields an output amplitude $V^2/2$ which is proportional to the point-source flux density F_ν . *Image Credit:* National Radio Astronomy Observatory.

sinusoidal oscillations are called fringes, and the fringe phase is

$$\phi = \omega \tau_g = \frac{\omega b \cos \theta}{c} \quad (1.19)$$

which changes with source direction as follows

$$\frac{d\phi}{d\theta} = \frac{\omega b \sin \theta}{c} = 2\pi \left(\frac{b \sin \theta}{\lambda} \right). \quad (1.20)$$

The fringe phase completes a full period (i.e., $\Delta\phi = 2\pi$) when an angular change $\Delta\theta = (\lambda/b \sin \theta)$ occurs. This tells us that the fringe phase is an extremely sensitive measure of source position if the projected baseline $b \sin \theta$ is many wavelengths long

1.3 Fundamentals of Radio Interferometry

and is the reason why interferometers can determine the positions of compact radio sources with exquisite accuracy.

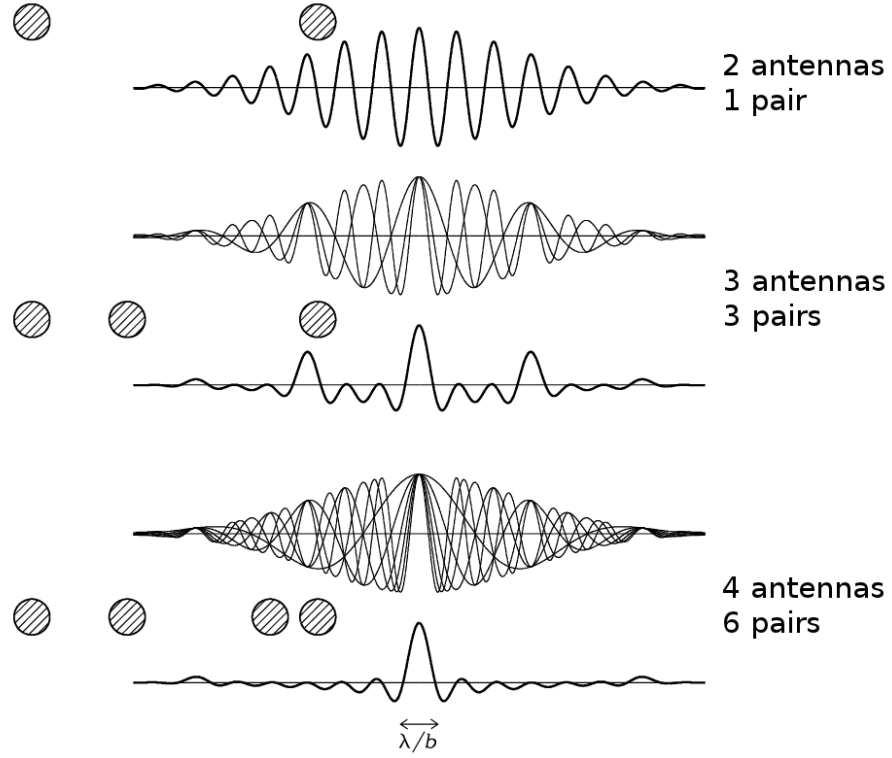


Figure 1.7: The instantaneous point source responses of an interferometer with two, three and four elements is indicated by the thick curves. The individual responses of the three pairs of two-element interferometers of the three-element interferometer and the six pairs of two-element interferometers of the four-element interferometer are plotted as thin curves. The main beam of the four-element interferometer is nearly Gaussian and has a width of $\sim \lambda/B$. This is known as the instantaneous synthesized beam of the interferometer. *Image Credit:* National Radio Astronomy Observatory.

If the antennas in an interferometric array are isotropic, then the point-source response of the interferometer would be a sinusoid spanning the entire sky and the interferometer would be only sensitive to one Fourier component of the sky brightness distribution having angular period $\lambda/b\sin\theta$. The response of a two-element interferometer R with non-isotropic antennas is this sinusoid multiplied by the product of the voltage patterns (i.e., defined as $f(u, v)$ in Section 1.1.1)

1.3 Fundamentals of Radio Interferometry

of the individual antennas. If the antennas are identical then this product is the power pattern of the individual antennas called the primary beam. The primary beam is usually a Gaussian that is much wider than the fringe period as $D \ll b \sin \theta$. The result is that an interferometer with directive antennas responds to a finite range of angular frequencies centered on $b \sin \theta / \lambda$. The instantaneous point source response of an interferometer is known as the synthesized beam and is the point source response obtained by averaging the outputs of all antenna pairs. The synthesized beam of an interferometer is an important quantity as it defines the maximum angular resolution of the instrument. The synthesized beams produced by an interferometer with a various number of antennas arranged in 1-D is shown in Figure 1.7. The figure shows that the synthesized beam can be improved by acquiring more Fourier components (i.e., baselines) and rapidly approaches a Gaussian as N increases. However, sidelobes are still significant and a broad negative “bowl” exists between the main beam and the first sidelobes due to the absence of short spacings.

1.3.3 Complex Visibility

The interferometer output can be expressed in terms of the radio brightness over the sky, which is sometimes also called specific intensity and has units $\text{W m}^{-2} \text{Hz}^{-1} \text{sr}^{-1}$. If the radio brightness of a spatially incoherent extended source in the direction of unit vector \mathbf{s} is $I(\mathbf{s})$, then the response of the two-element interferometer with “cosine” correlator output near frequency $\nu = \omega/2\pi$ is obtained by treating the extended source as the sum of independent point sources:

$$R_c = \int_{\Omega} \mathcal{A}(\mathbf{s}) I_{\nu}(\mathbf{s}) \cos \left(\frac{2\pi \mathbf{b} \cdot \mathbf{s}}{\lambda} \right) d\Omega \quad (1.21)$$

where \mathcal{A} is the normalized antenna reception pattern defined in Section 1.1.1 and we call $\mathcal{A}(\mathbf{s}) I_{\nu}(\mathbf{s})$ the modified brightness distribution. However, the cosine function in the “cosine” correlator output is only sensitive to the even part of the sky brightness distribution, which can be written as the sum of even and odd parts:

$$I(\mathbf{s}) = I_e(\mathbf{s}) + I_o(\mathbf{s}). \quad (1.22)$$

1.3 Fundamentals of Radio Interferometry

A “sine” correlator whose output is odd, is needed to detect the odd part of $I(\mathbf{s})$ and this is implemented by inserting a 90° phase delay into the signal of one of the antennas to give

$$R_s = \int_{\Omega} \mathcal{A}(\mathbf{s}) I_{\nu}(\mathbf{s}) \sin\left(\frac{2\pi \mathbf{b} \cdot \mathbf{s}}{\lambda}\right) d\Omega \quad (1.23)$$

It is convenient to write the cosines and sines as complex exponentials using the identity

$$e^{i\phi} = \cos(\phi) + i\sin(\phi) \quad (1.24)$$

and so the combination of “cosine” and “sine” correlators is called a “complex” correlator. The term *visibility* was first introduced by [Michelson \(1890\)](#) to describe the relative amplitudes of the optical fringes that he observed. The visibility is a complex quantity in radio astronomy and has dimensions of spectral power flux density ($\text{W m}^{-2} \text{Hz}^{-1}$). The complex visibility is the response of a two-element interferometer with a complex correlator to an extended source with brightness distribution $I(\mathbf{s})$ and is defined as

$$V \equiv R_c - iR_s, \quad (1.25)$$

i.e.,

$$V_{\nu} = \int_{\Omega} \mathcal{A}(\mathbf{s}) I_{\nu}(\mathbf{s}) e^{-2\pi i \nu \mathbf{b} \cdot \mathbf{s} / c} d\Omega. \quad (1.26)$$

1.3.4 Coordinate Systems for Imaging

The baseline vector \mathbf{b} has coordinates (u, v, w) in three dimensions shown in Figure 1.8 where w points in the directions of interest, i.e., towards a direction s_0 that becomes the center of the synthesized image. u , v and w are measured in wavelengths (i.e., the components of \mathbf{b}/λ) and have directions towards the East, the North and the phase tracking center, respectively. An arbitrary unit vector \mathbf{s} has components (l, m, n) called direction cosines, where $n = \cos\theta =$

$(1 - l^2 - m^2)^{1/2}$. Using these coordinates the parameters in Equation 1.26 become

$$\begin{aligned}\frac{\nu \mathbf{b} \cdot \mathbf{s}}{c} &= ul + vm + wn, \\ d\Omega &= \frac{dl dm}{n} = \frac{dl dm}{\sqrt{1 - l^2 - m^2}}.\end{aligned}\tag{1.27}$$

Therefore Equation 1.26 can be defined in terms of the coordinate system laid out in Figure 1.8 as

$$V_\nu(u, v, w) = \int_{-\infty}^{\infty} \int_{-\infty}^{\infty} \mathcal{A}_\nu(l, m) I_\nu(l, m) e^{-2\pi i [ul + vm + w(\sqrt{1 - l^2 - m^2})]} \frac{dl dm}{\sqrt{1 - l^2 - m^2}}\tag{1.28}$$

which is not a three-dimensional Fourier transform. This equation becomes a two-dimensional Fourier transform if $w = 0$ which is a good approximation for small field imaging, i.e., when $|l|$ and $|m|$ are small. Thus, for an incoherent source in the far field observed with a small FOV and ignoring the response of the primary beam, the complex visibility is the 2-dimensional Fourier Transform of the sky brightness distribution

$$V_\nu(u, v) = \int_{-\infty}^{\infty} \int_{-\infty}^{\infty} I_\nu(l, m) e^{-2\pi i [ul + vm]} dl dm.\tag{1.29}$$

This Fourier transform relationship is the result of the van Cittert-Zernike theorem (van Cittert, 1934), upon which synthesis imaging is based. Since $I_\nu(l, m)$ is real, $V(u, v)$ is Hermitian [i.e., $V(-u, -v) = V^*(u, v)$] and so one measurement of the sky brightness gives two measurements of the complex visibility. Also, $V(u = 0, v = 0)$ is the integral of $I_\nu(l, m) dl dm$, which is the total flux. An interferometer cannot measure this value because it cannot take measurements at $(u = 0, v = 0)$.

1.4 Synthesis Imaging

A synthesis imaging telescope consists of a number radio antennas fixed on the ground and uses the Earth's rotation to vary the projected baseline coverage to increase the sampling of the $u - v$ plane. In this section we describe how Earth-

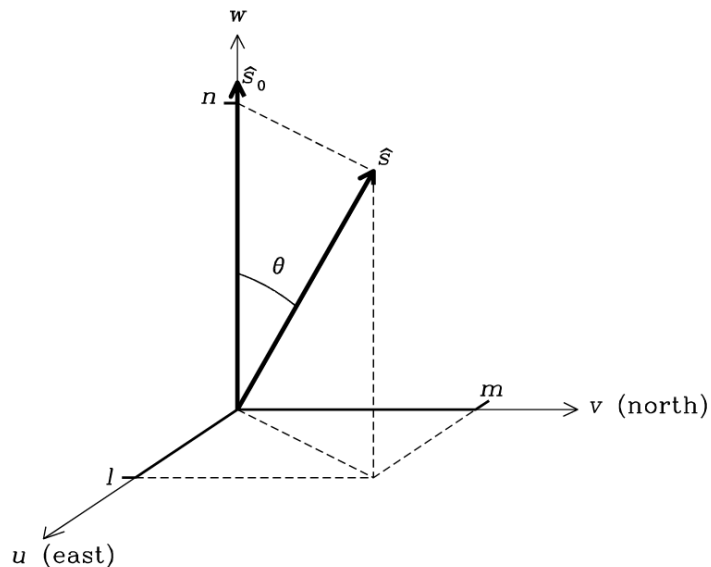


Figure 1.8: The (u, v, w) interferometric coordinate system. l , m , and n are the projections of the unit vector \mathbf{s} onto the u , v , and w axes, respectively.

rotation aperture synthesis is used to convert the complex visibilities outputted from the correlator to a final radio image of the observed sky.

1.4.1 Visibility Sampling

An example of how a radio interferometer samples the $u - v$ plane is shown in Figure 1.9. The left panel of this figure shows the overhead view of the VLA in its most extended configuration while the other two panels shows the corresponding $u - v$ coverage for different periods of time. We define u and v as the east-west and north-south components of the projected baseline in wavelengths, respectively. As the Earth rotates, the projected baseline of every two-element pair in the array changes, thus sampling a different part of the $u - v$ plane. The middle panel shows that the total $u - v$ coverage of the VLA for a very short duration track (i.e., a snapshot) results in a ‘snowflake’ like pattern, with more dense coverage in the direction of the arms of the array due to the larger number of baselines. Most radio interferometers have their own unique array configuration layout and thus produce a different ‘snapshot’ $u - v$ coverage to that shown in Figure 1.9. Over many hours, the $u - v$ points trace out portions of ellipses and eventually

after a full Earth rotation the points can trace out full ellipses as shown in the right panel of Figure 1.9.

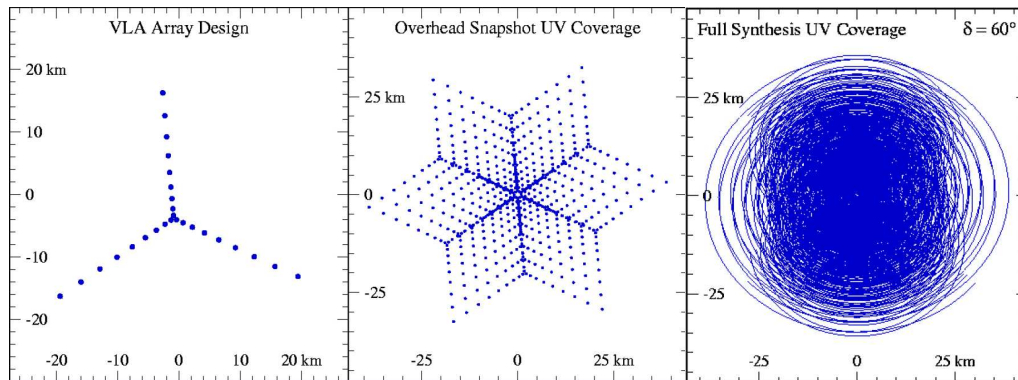


Figure 1.9: *Left:* The VLA in A-configuration is an example of an ‘Y’ shaped array design. *Middle:* The corresponding overhead snapshot $u-v$ coverage results in ‘snowflake’ pattern. *Right:* The corresponding $u-v$ coverage after a 12 hour track of a source at a declination of 60° . Note the more intense $u-v$ coverage in the direction of the three straight arms of the VLA for a snapshot track compared to the more uniform coverage over a longer duration track.

1.4.2 Imaging (Making a Dirty Map)

For every sky brightness distribution $I(l, m)$ there exists a continuous complex visibility function $V(u, v)$ that is its Fourier Transform. An array of antennas will only ever measure a certain set of values of this visibility function where the measured set is called the sampling function $S(u, v)$. This function is zero where no data have been taken. The actual data provided by the array is known as the sampled visibility function, $S(u, v)V(u, v)$. If we take the inverse Fourier transform of this function we get what is known as the *dirty image*:

$$I_\nu^D(l, m) = \int_{-\infty}^{\infty} \int_{-\infty}^{\infty} S(u, v) V_\nu(u, v) e^{2\pi i(ul + vm)} du dv. \quad (1.30)$$

where we have used $I_\nu(l, m)$ to denote the modified sky brightness $\mathcal{A}(l, m)I_\nu(l, m)$ as the correction for primary beam can be made at the final stage of data processing. Using the convolution theorem, the relationship between the dirty image

and the desired intensity distribution $I_\nu(u, v)$ is

$$I_\nu^D(u, v) = I_\nu(u, v) * B(l, m) \quad (1.31)$$

where the asterisk implies convolution and

$$B(l, m) = \int_{-\infty}^{\infty} \int_{-\infty}^{\infty} S(u, v) e^{2\pi i(ul+vm)} du dv \quad (1.32)$$

is the *point spread function* (PSF), or *synthesized beam*, or *dirty beam* (i.e., the inverse Fourier Transform of the sampling function S). Equation 1.31 says that the dirty image I^D is the true intensity distribution I , convolved with the synthesized beam B .

In Figure 1.10 we graphically summarize what has been said above. The panels in the upper row show the sky plane representations of the true image, the point spread function and the dirty image, while the panels in the lower row show the corresponding $u - v$ plane representations of the true visibility, the sampling function and the sampled visibility. In other words, Equation ?? is summarized graphically by the relationship between panels (a) and (d), Equation 1.32 by (b) and (e), and Equations 1.30 and 1.31 by (c) and (f).

Before the dirty image is computed, a weighting system is often applied to the visibilities to control the PSF. The two most common types of weighting system used are:

$$D_k = 1, \quad \text{natural weighting} \quad (1.33)$$

$$D_k = \frac{1}{N_s(k)}, \quad \text{uniform weighting} \quad (1.34)$$

where D_k is the weight to be applied to cell k , and $N_s(k)$ is the number of data samples falling into cell k of characteristic width s . Natural weighting treats all points alike and gives the best signal-to-noise ratio for detecting weak sources. However, it produces a beam with a broad low-level plateau which is undesirable when imaging sources with both large and small scale structure. Uniform gridding produces fewer artifacts in the final map, while keeping the full resolution of the array but gives poorer signal-to-noise than natural weighting.

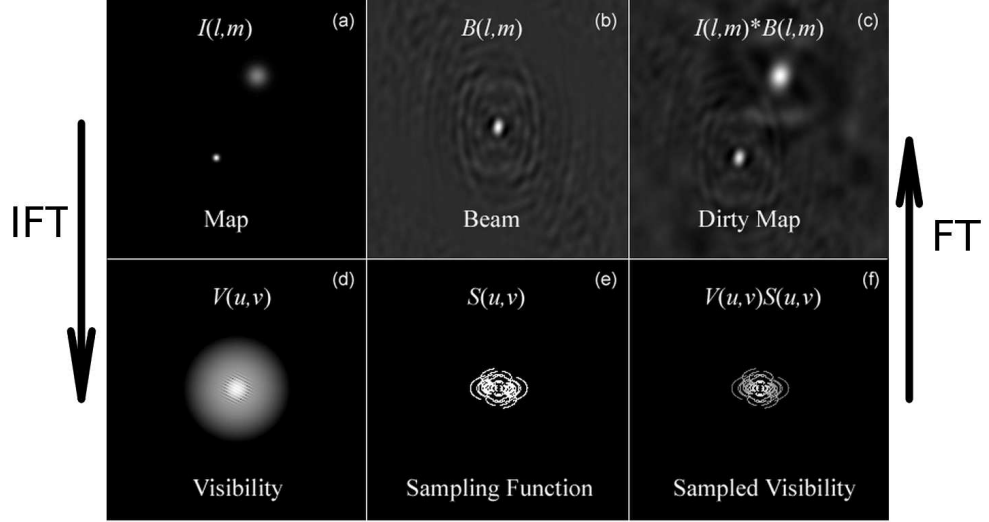


Figure 1.10: The Fourier transform pairs in synthesis imaging. (a) and (d): The true sky brightness and the visibility. (b) and (e): The dirty beam and the sampling function. (c) and (f): The dirty image and the sampled visibility. *Image Credit:* Prof. Dale E. Gary (New Jersey Institute of Technology).

The ‘direct Fourier transform’ method can then be used to solve for the dirty image Equation 1.30. However, if this method is evaluated at every point on a $N \times N$ grid, then the number of multiplications required goes as N^4 . The fast Fourier transform (FFT) algorithm can also be used to solve Equation 1.30 but requires interpolating the data onto a regular grid (i.e., a process known as *gridding*). This method is widely used for large data volumes as it requires only a few times $N^2 \log_2 N$ operations - not $\mathcal{O}(N^4)$, and the total time taken for gridding and FFT is usually a lot less than would take using the direct Fourier transform method.

1.4.3 Deconvolution (Making a CLEAN map)

The solution to the inverse Fourier transform given in Equation ?? is not unique, because the unmeasured points in the $u - v$ plane could have *any* value without violating the data constraints. The ‘principle solution’ is the one in which all missing $u - v$ measurements are set to zero and gives the dirty image discussed in the previous section. The dirty image is usually not a satisfactory representation

of the sky as one would expect a more continuous distribution of visibilities than that provided by the array. The goal of the deconvolution process is to find a method that determines more reasonable values for the unmeasured $u - v$ data. A priori information is the key to choosing ‘reasonable’ values. For example, we know that the Stokes parameter I must be positive and that radio sources generally do not have sidelobe patterns.

The CLEAN algorithm (Cornwell *et al.*, 1999; Högbom, 1974; Schwarz, 1978) is the most widely used technique in radio interferometry to deconvolve the true sky intensity from the dirty beam. It assumes that the radio source can be represented by a number of point sources in an otherwise empty field and a simple iterative process is used to find the strengths and positions of these point sources. The final CLEAN image (i.e., the deconvolved image) is the sum of these point sources convolved with a CLEAN beam, which is usually an elliptical Gaussian of the same size and shape as the inner part of the dirty beam. The CLEAN algorithm obeys the following steps:

1. Find the strength and position of the brightest point in the dirty image. It may also be desirable to search for peaks in specified areas of the image, called CLEAN windows or regions.
2. At this position in the dirty image, subtract the dirty beam multiplied by the peak strength and a damping factor g ($g \leq 1$, usually called the loop gain).
3. Record the position and the subtracted flux in a model.
4. Iterate between (1), (2), and (3) until the peak is below some user specified level. The remainder of the dirty image is now termed the residuals.
5. Convolve the accumulated point source model with an idealized CLEAN beam (usually an elliptical gaussian of the same size and shape as the central lobe of the dirty beam).
6. Add the residuals to the image in (5) to create the final CLEAN image.

A problem with CLEAN is that the final CLEANed image is somewhat dependent upon the various control parameters such as CLEAN boxes, the loop gain and the number of CLEAN subtractions. For example, using too high a gain tends to make extended, weak emission undetectable and noisy. This problem is unavoidable, and input values must be chosen on a case by case basis, depending on the source and data quality.

Another deconvolution algorithm used in radio synthesis imaging, albeit less often, is the Maximum Entropy Method (MEM) which operates by minimizing a smoothness function (‘entropy’) in an image. To conclude this section, we briefly discuss the practical differences between CLEAN and MEM:

1. CLEAN is nearly always faster than MEM, unless the image contains more than 1 million pixels.
2. MEM images are nearly always smoother than CLEAN images. This is because for CLEAN, what happens at one pixel is not coupled to what happens to its neighbours, while MEM couples pixels together by minimizing the spread in pixel values.
3. CLEAN sometimes makes extended emission look blotchy and may introduce artificial stripes into the image while MEM copes very poorly with point sources in extended emission. (Multi-scale CLEAN which is discussed in Chapter ?? is now becoming a popular choice in the radio community as an alternative deconvolution algorithm for images containing extended emission.)
4. For MEM, it is necessary to know the noise level quite well and it also helps to know the total flux density of the image. Knowledge of these are not required for CLEAN.



List of Abbreviations Used in this Thesis.

Table A.1: List of Abbreviations

Acronym	Meaning
ALMA	The Atacama Large Millimeter/submillimeter Array
AGB	Asymptotic Giant Branch
ALC	Automatic Level Control
BIMA	Berkeley Illinois Maryland Association
CARMA	Combined Array for Research in Millimeter-wave Astronomy
CASA	Common Astronomy Software Application
CSE	Circumstellar Envelope
DDT	Director's Discretionary Time
e-MERLIN	e-Multi-Element Radio Linked Interferometer Network
FITS	Flexible Image Transport System
FOV	Field of View
GHRS	Goddard High-Resolution Spectrograph
GREAT	German Receiver for Astronomy at Terahertz Frequencies
HPBW	Half Power Beamwidth
H-R	Hertzsprung-Russell
HST	Hubble Space Telescope
IOTA	Infrared Optical Telescope Array
IR	Infrared

Continued on next page

Table A.1 – *Continued from previous page*

Acronym	Meaning
IRAM	Institut de Radioastronomie Millimétrique
IUE	International Ultraviolet Explorer
LSR	Local Standard of Rest
LTE	Local Thermodynamic Equilibrium
MEM	Maximum Entropy Method
MERLIN	Multi-Element Radio Linked Interferometer Network
MHD	Magnetohydrodynamic
OVRO	Owens Valley Radio Observatory
OSRO	Open Shared Risk Observing
RF	Radio Frequency
RFI	Radio Frequency Interference
RGC	Red Giant Clump
RGB	Red Giant Branch
RSG	Red Supergiant
S/N	signal-to-noise ratio
SB	Scheduling Block
SGB	Subgiant Branch
SOFIA	Stratospheric Observatory for Infrared Astronomy
SMA	Submillimeter Array
SZA	Sunyaev-Zel'dovich Array
SIS	superconductorinsulatorsuperconductor
UV	Ultraviolet
VLA	Karl G. Jansky Very Large Array
VLBA	Very Long Baseline Array
VLT	Very Large Telescope
W-R	Wolf-Rayet

References

- CORNWELL, T., BRAUN, R. & BRIGGS, D.S. (1999). Deconvolution. In G.B. Taylor, C.L. Carilli & R.A. Perley, eds., *Synthesis Imaging in Radio Astronomy II*, vol. 180 of *Astronomical Society of the Pacific Conference Series*, 151. (Cited on page 24.)
- HÖGBOM, J.A. (1974). Aperture Synthesis with a Non-Regular Distribution of Interferometer Baselines. *Astronomy & Astrophysics Supplement*, **15**, 417. (Cited on page 24.)
- JACKSON, N. (2008). Principles of Interferometry. In F. Bacciotti, L. Testi & E. Whelan, eds., *Jets from Young Stars II*, vol. 742 of *Lecture Notes in Physics*, Berlin Springer Verlag, 193. (Cited on pages 12 and 14.)
- KRAUS, J.D., TIURI, M., RAISANEN, A.V. & CARR, T.D. (1986). *Radio astronomy receivers*. (Cited on page 3.)
- MICHELSON, A.A. (1890). . *Phil. Mag.*, **30**, 1–21. (Cited on page 18.)
- SCHWARZ, U.J. (1978). Mathematical-statistical Description of the Iterative Beam Removing Technique (Method CLEAN). *Astronomy & Astrophysics*, **65**, 345. (Cited on page 24.)
- TAYLOR, G.B., CARILLI, C.L. & PERLEY, R.A., eds. (1999). *Synthesis Imaging in Radio Astronomy II*, vol. 180 of *Astronomical Society of the Pacific Conference Series*. (Cited on pages 7 and 8.)
- VAN CITTERT, P.H. (1934). Die Wahrscheinliche Schwingungsverteilung in Einer von Einer Lichtquelle Direkt Oder Mittels Einer Linse Beleuchteten Ebene. *Physica*, **1**, 201–210. (Cited on page 19.)